Plant Cell wall inspired Xyloglucan/Cellulose Nanocrystals Aerogels Produced By Freeze-Casting

Z. Jaafar, B. Quelennec, C. Moreau, D. Lourdin, J.E. E Maigret, B. Pontoire, A. D'orlando, T. Coradin, Benoît Duchemin, F.M. Fernandes, et al.

Plant Cell wall inspired Xyloglucan/Cellulose Nanocrystals Aerogels Produced By Freeze-Casting

*Z. JAAFAR[1], B. QUELENNEC[1], C. MOREAU[1], D. LOURDIN[1], J. E. MAIGRET[1], B. PONTOIRE[1], A. D'ORLANDO[1-4], T. CORADIN[2], B. DUCHEMIN[3], F.M. FERNANDES[2], B. CATHALA[1]**

1 INRAE, UR BIA, F-44316, Nantes, France

2 Sorbonne Université, CNRS, Laboratoire de Chimie de la Matière Condensée de Paris, 75005 Paris, France

3 Normandie Université, ULH, CNRS, LOMC, 76600 Le Havre, France

4 INRAE, BIBS-UR BIA, F-44316, Nantes, France

HIGHLIGHTS

- Non-directional and directional freezing of CNC/xyloglycan aerogels is reported
- Addition of xyloglycan (XG) changes aerogel morphology from lamellar to alveolar
- Directional freeze-casting leads to oriented pores ehancing mechanical properties
- Increasing CNC/XG ratio improves mechanical properties of aerogels
- Without chemical cross-linking, such CNC/XG aerogels do not dispersed in water

GRAPHICAL ABSTRACT:

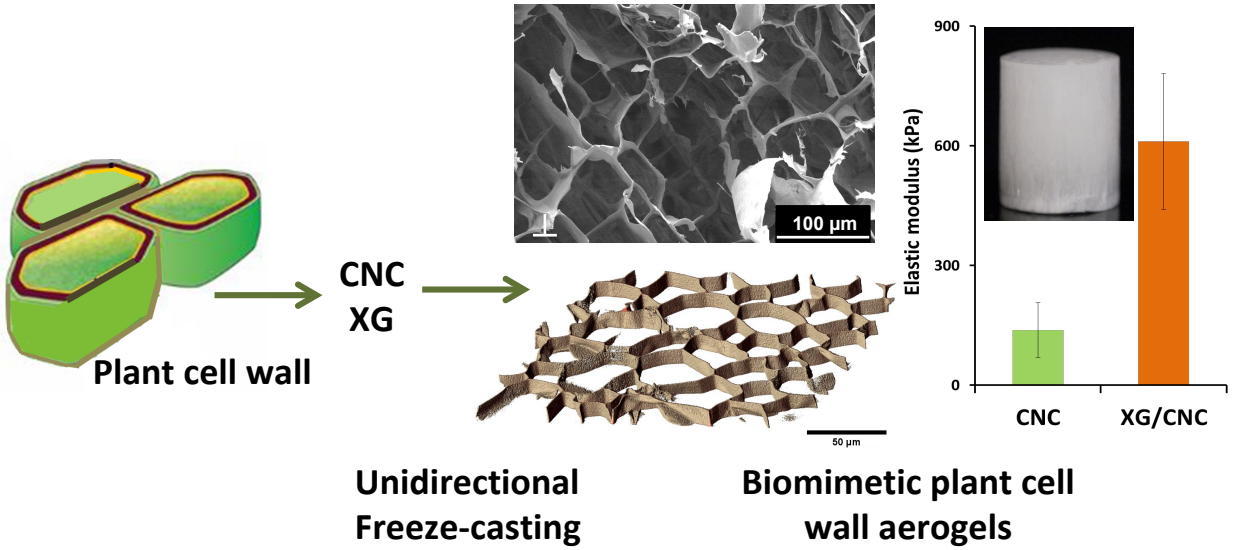

ABSTRACT

Cellulose nanocrystals (CNC) and xyloglucan (XG) were used to construct new aerogels inspired by the hierarchical organization of wood tissue, i.e., anisotropic porous cellular solid with pore walls containing oriented and stiff cellulose nanorods embedded in hemicellulose matrix. Aerogels with oriented or disordered pores were prepared by directional and non-directional freeze-casting from colloidal dispersions of XG and CNC at different ratios. XG addition induced a clear improvement of the mechanical properties compared to the CNC aerogel, as indicated by the Young modulus increase from 138 kPa to 610 kPa. The addition of XG changed the pore morphology from lamellar to alveolar and it also decreased the CNC orientation (the Hermans' orientation factor was 0.52 for CNC vs 0.36-0.40 for CNC-XG). The aerogels that contained the highest proportion of XG also retained their structural integrity in water without any chemical modification. These results open the route to biobased water-resistant materials by an easy and green strategy based on polymer adsorption rather than chemical crosslinking.

KEYWORDS: xyloglucan (XG), cellulose nanocrystal (CNC), directional freeze-casting, aerogel, mechanical property

1 INTRODUCTION

Plant stem tissues are highly organized, hierarchical structures. At the tissue level, cells form an anisotropic and porous cellular structure that is oriented along the stem (Cosgrove, 2005; Svagan, Jensen, Dvinskikh, Furó, & Berglund, 2010). Cell walls are themselves nanostructured since they consist of oriented cellulose nanofibers along the long axis of the fibers and organized in a helicoidal manner. This structural hierarchy is largely responsible for the remarkable mechanical properties of plant cell walls that also display low density and resistance to pathogens and other stresses (Burgert, 2006; Lakes, 1993). The main cell wall components, namely cellulose, hemicellulose and lignin, form a complex network in which they act cooperatively and thereby determine the mechanical behavior of the entire cell wall (Burgert, 2006; Cosgrove, 2005). The whole structural role of hemicelluloses in the cell wall is not fully established, but hemicelluloses are considered to contribute to load transfer and connecting cellulose fibers (Lopez-Sanchez et al., 2015).

Cellulose nanocrystals (CNC) are rod-like nanoparticles prepared by the removal of disordered parts of cellulose fibers (Klemm et al., 2011). Because of their impressive mechanical properties and nanometric dimensions, they have recently been used as reinforcement materials in composite films, hydrogels and aerogels (Karaaslan, Tshabalala, Yelle, & Buschle-Diller, 2011; Saxena, Elder, Pan, & Ragauskas, 2009). Xyloglucans (XG) are hemicelluloses displaying a large structural variability present in the primary plant cell wall. XG is believed to contribute to the

mechanical properties of the plant cell walls (Cosgrove, 2014; Scheller & Ulvskov, 2010), since XG has a high affinity to cellulose and adsorbs irreversibly on cellulosic surfaces (Cosgrove, 2014). It has been shown that XG adopts different conformations when adsorbed on CNC, depending on the CNC/XG concentration ratios: at low ratios, almost all XG chains bind as trains to the CNC surface, whereas at high ratios, XG forms more loops and tails (Dammak et al., 2015; Villares, Moreau, Dammak, Capron, & Cathala, 2015). Here, we hypothesize that such conformational variations might affect the properties of cellulose/XG assemblies.

Aerogels are materials derived from hydrogels in which the liquid phase has been replaced by a gas in mild conditions. They are characterized by a very high porous volume (> 90%) and display interesting properties (Fricke & Tillotson, 1997). Among the different techniques used to create porous materials, freeze-casting is a versatile and easy to implement technique. Freeze-casting involves unidirectional freezing of a colloidal suspension or a solution following a predefined thermal gradient (Deville, 2010). In water, due to the limited solubility of most compounds in ice, most solutes and/or suspended particles are segregated from the growing ice front into the interstitial space defined by ice crystals. Subsequent solvent sublimation leads to the formation of aerogels whose porosity reproduces the ice crystals' morphology (Deville, 2008). Bioaerogels, *i.e.* aerogels prepared from natural materials, with homogeneous and well-defined architectures have been a subject of primary interest because of their potential applications in areas such as thermal insulation (Wicklein et al., 2015), tissue engineering (Ghorbani, Nojehdehian, & Zamanian, 2016; Yin, Divakar, & Wegst, 2019), drug delivery (Szepes, Ulrich, Farkas, Kovács, & Szabó-Révész, 2007) and automotive components (Köhnke, Lin, Elder, Theliander, & Ragauskas, 2012; Lee & Deng, 2011). It was found that the distribution of pore size, pore shape and pore connectivity is the result of the shape of ice crystals formed during freezing (Jiménez-Saelices, Seantier, Grohens,

& Capron, 2018). Hence, different microstructures and associated functional properties can be obtained by controlling operating parameters such as the freezing rate (or ice front velocity), the interfacial free energy between the particles and the liquid, the interaction of the particles with themselves, as well as the size, distribution and concentration of the particles (Deville, Saiz, & Tomsia, 2006).

A number of CNC aerogels prepared by freeze-casting have been reported in the literature (Chau et al., 2016; Chu, Qu, Zussman, & Xu, 2017; Dash, Li, & Ragauskas, 2012; Munier, Gordeyeva, Bergström, & Fall, 2016). However, only few studies have focused on CNC-hemicelluloses hydrogels (Karaaslan et al., 2011; Köhnke, Elder, Theliander, & Ragauskas, 2014; Lopez-Sanchez et al., 2015) or aerogels (De France, Hoare, & Cranston, 2017; Köhnke et al., 2014; Köhnke et al., 2012). These examples, however, rely on chemical modification of CNC or hemicelluloses in order to promote polymer-polymer interactions. In contrast, the present study is devoted to the use of XG and CNC without any chemical pretreatment, taking advantage of their physical interactions and of the different conformations of XG adsorbed on CNC (Dammak et al., 2015). These conformations were controlled by varying the CNC/XG concentration ratios (Dammak et al., 2015) in order to develop bioaerogels with cellular structures that mimic the structural and mechanical properties of the plant cell wall (Kam et al., 2019; Pan et al., 2016). In order to elucidate the interplay between CNC/XG interactions and the properties of freeze-cast materials, they were compared to reference aerogels of the same composition obtained by non-directional freezing. With the aim of providing an integrated vision of these CNC/XG aerogels, we combined a multiscale (from nano- to macro-scale) structural approach using X-ray diffraction (XRD) to assess the orientation of the CNCs, scanning electron microscopy and confocal microscopy to investigate the porous structure, mechanical testing and water immersion conditions to study their

physical and chemical stability. On this basis, it was possible to unveil the multifaceted influence of XG on the macroscopic properties of biobased and biological materials.

2 MATERIALS AND METHODS

2.1 Chemicals

CNCs obtained from acid hydrolysis of bleached softwood kraft pulp were provided by CelluForce (Montreal, Canada). Product specifications are the following : crystalline fraction = 0.88 (by XRD), surface charge density = 0.023 mmol/g (by conductivity), lateral dimension = 2.3-4.5 nm (by AFM), length = 44-108 nm (by AFM). Aqueous CNC suspension (60 $g.L^{-1}$) was prepared by dispersing the CNC powder in deionized water (18.2 $M\Omega.cm^{-1}$, Millipore Milli-Q purification system) under vigorous stirring with a magnetic stirring bar overnight until it appeared to be well-dispersed according to visual inspection. Afterwards, the dispersion was sonicated for 10 min in an ice bath to avoid overheating, using a QSonica Q700 sonicator (20 kHz, QSonica LLC, Newtown, USA) with a 12.7 mm in diameter ultrasound probe (50 W with 50% amplitude).

Xyloglucan from *Tamarindus indica* was provided by Megazyme (Bray, County Wicklow, Ireland). Monosaccharide composition (dry weight %): Glucose 49.1 ± 1.1; Xylose 32.1 ± 2.3; Galactose 16.4 ± 0.6; Arabinose 2.4 ± 0.1. The mass average molar mass was $\overline{M_w}$ = 840 × 10^3 $g.mol^{-1}$ and the number average molar mass was $\overline{M_n}$ = 677 × 10^3 $g.mol^{-1}$ (dispersity $Đ$ = 1.24). A XG solution with a 10 $g.L^{-1}$ concentration was first prepared. It was then concentrated to 20 $g.L^{-1}$ by osmosis in a dialysis membrane (Espectra/Por®, cutoff 6–8 kDa) immersed in a 10 wt.% aqueous dextran solutions (10^5 $g.mol^{-1}$).

2.2 Aerogel preparation

148 The final concentration of the CNC/XG suspensions was fixed at 2 wt.% dry matter and this
149 concentration was kept constant independently of the CNC:XG ratio. CNC-XG complexes were
150 prepared by mixing dispersed CNC and XG at two different concentration ratios: 1.9/0.1 wt.% and
151 1.6/0.4 wt.% CNC/XG. The mixtures were respectively denoted CNC1.9 XG0.1 and CNC1.6
152 XG0.4 (Figure 1) and they were left under stirring for 18 h. CNC and CNC/XG aerogels were
153 prepared using unidirectional (UF) and non-directional (NF) freeze-casting methods. The UF
154 device was built in our laboratory according to the literature[34,35] and consisted of a liquid nitrogen
155 Dewar, a copper bar, a heating element and a polypropylene tube partially inserted in the hot end
156 of the copper bar to hold the sample prior to freezing. It was assembled in such a way that half of
157 the copper bar was plunged into liquid N_2 to create a heat sink. In a typical experiment, 3 mL of
158 the 2 wt.% CNC-XG mixture was poured in the polypropylene tube, in direct contact with the
159 copper surface. After a 5-min equilibration time at 20 °C, the sample was cooled down to -60 °C
160 at a cooling rate of -1 °C.min^{-1}, and then removed from the device and placed at -20 °C before
161 freeze-drying for 24 h. NF experiments were examined by placing dispersions in a freezer (-20 °C)
162 for approximately 3 h. All the samples were cylinders with a mean diameter (D) of ≈ 10 mm and
163 a mean initial height (h) of ≈ 20 mm.
164 Ice sublimation was conducted in a Christ Alpha 2-4 LD freeze dryer. The temperature of the
165 freeze dryer condenser was kept below -60°C and the internal pressure stabilized within few
166 minutes to approximately 5.10^{-5} bar. The freeze-drying process was left to proceed for 24 h,
167 allowing for the recovery of a dried lightweight solid.
168 The bulk density $\rho_{aerogel}$ of the aerogels was calculated by dividing their weight by their
169 volume. The weight of aerogels was determined with an analytical balance (Mettler Toledo XS),
170 and their volume was measured with a digital caliper. The void fraction (%) of the aerogel was

171 calculated using the equation below where the density of cellulose is: 1500 kg.m^{-3}.

172 $$\Phi = \left(1 - \frac{\rho_{aerogel}}{\rho_{CNC}}\right) * 100 \qquad (1)$$

173 To visualize the structure of the aerogels, the foams were manually cut with new scalpel blades.
174 Scanning electron microscopy (SEM) observations were performed on a Thermo Fisher Quattro
175 S. The samples were sputter-coated with 5 nm of platinum and observed under 3-4 kV acceleration
176 and 30 μA probe current.

177

178 2.3 Fluorescent labeling of XG and CNC and confocal microscopy

179 Labeling was achieved according to the protocol reported by Berder *et al.*(de Belder & Granath,
180 1973). Briefly, XG or CNC (1 g) were dissolved/dispersed under stirring in 40 mL of
181 dimethysulfoxide containing a few drops of pyridine at 65°C, then 10 mg of fluorescein
182 isothiocyanate (FITC) or rhodamine B isothiocyanate (RBITC) were added with 50 µL of
183 dibutyltin dilaurate. The mixture was heated during 2 hours at 95°C. The solution/suspension was
184 poured in ethanol and the precipitate was resuspended several time in acetone and precipitated
185 again to remove the unbound dye. The precipitate was then dissolved in water and dialyzed against
186 ultra pure water until no UV signal of free dye was detected in the washing solutions. CNC and
187 XG suspensions/solutions were then concentrated by osmosis as described above. The aerogels
188 were also prepared according to the same protocols as described above.

189 Confocal microscopy was performed on a Leica SP5 upright microscope using a Leica HPX CL
190 Apochromat 63x 1.4 oil objective. Samples were sliced perpendicular to the ice growth direction
191 (thickness inferior to 1mm) followed by immersion in oil before imaging. The immersion of
192 samples in oil enabled refractive index matching between the objective, the glass coverslips and
193 the sample porous volume thus minimizing optical refraction and maximizing resolution. No

194 dissolution or deformation of the foams could be noticed when performing the oil immersion.
195 Sequential images were acquired in 300 nm z steps. Image analysis was conducted in FIJI software
196 using the Volume Viewer and Coloc2 plugins (Schindelin et al., 2012).
197
198 2.4 Mechanical testing
199 Longitudinal compression measurements were performed on the dry aerogels. Before testing, all
200 the aerogels were stored for at least one day in the measurement room in order to guarantee the
201 same conditions of temperature (20 °C) and humidity (RH= 35%). The mechanical properties were
202 characterized by uniaxial compression experiments in an MTS SYNERGIE 100 machine equipped
203 with a 100 N load cell. The compression tests were performed up to the maximum load and the
204 compression force was parallel to the temperature gradient used for the manufacturing of the UF
205 samples. The cylindrical samples were compressed between two steel plates. A deformation rate
206 of 3 $mm.min^{-1}$ was applied on the top surface of each specimen until the deformation of the sample
207 exceeded 70%. The corresponding stress-strain curves were obtained for five replicas per sample.
208 2.5 Determination of CNC orientation by X-ray diffraction
209 The diffractograms were recorded on a Bruker-AXS D8 Discover diffractometer. The X-ray beam
210 was produced in a sealed copper tube at 40 kV and 40 mA. The 500-µm beam with a CuKα1
211 wavelength (1.5405 Å) was collimated and parallelized using two crossed-coupled Göbel mirrors.
212 The X-ray diffraction data were collected using a Vantec 500 two-dimensional detector in the 3-
213 40° 2.θ range. The samples were placed perpendicular or parallel to the X-ray beam.
214 The azimuthal intensity profiles were used in the calculation of the Herman's orientation factor
215 defined by (Hermans, Hermans, Vermaas, & Weidinger, 1946):
216 $$f = [3\ (cos^2\chi) - 1]/2 \qquad (2)$$

Where f is the crystal chain axis orientation factor and χ is the angle between the chain axis and the reference direction. The value of $cos^2\chi$ is computed from the azimuthal angular distribution of XRD intensity profile by:

$$cos^2(\chi) = \frac{\sum_0^{\pi/2} I(\chi)\sin(\chi)cos^2(\chi)}{\sum_0^{\pi/2} I(\chi)\sin(\chi)} \qquad (3)$$

Where $I(\chi)$ Is the angular intensity profil from the XRD pattern. The degree of orientation f is the first term in the expansion of an orientation distribution function which depends on the angle between the chain axis and the reference direction. f is equal to 0 for random orientation and to 1 for a perfect alignement (Kim, Oh, & Islam, 2012).

2.6 Evaluation of dispersibility in water

The aerogels were immersed in deionized water containing one drop of blue ink for enhancing the visualization of the wet aerogel. The immersed aerogels were kept at 4°C and dispersion was visually evaluated every 12 hours. Photographs were taken at different characteristic times.

3 RESULTS

3.1 Aerogel preparation

Figure 1 gives a schematic description of the different compositions and freezing routes of the aerogels. All the aerogels were prepared by ice templating from suspensions of 2 wt% total polymer content. Two different CNC/XG concentration ratios, 1.9/0.1 wt% and 1.6/0.4 wt%, were selected corresponding to different adsorption regimes, below and above the required ratio to saturate the CNC surface with XG molecules, respectively (Dammak et al., 2015). Previously

reported saturation range is between 20-30 mg XG /g of CNC. Thus, for CNC1.9 XG0.1, the amount of XG is lower than that needed for CNC surface saturation. XG will strech to cover all the CNC surface available and adsorb in the train conformation. For the CNC1.6 XG0.4 mixture, XG is close to the saturation concentration. The CNC surface is fully covered, increasing the polymer crowding that will thus adsorb with more loops and tails. (Dammak et al., 2015) CNC2 XG0 aerogels were used as references. Aerogels were prepared by both NF where the ice crystals nucleate and grow randomly in diverse directions and UF where the suspension is exposed to a controlled cooling element inducing the growth of ice crystals along the generated thermal gradient (Figure 1) (Deville, 2008). Monolithic and homogeneous aerogels were successfully obtained from CNC/XG mixtures with the two freezing methods.

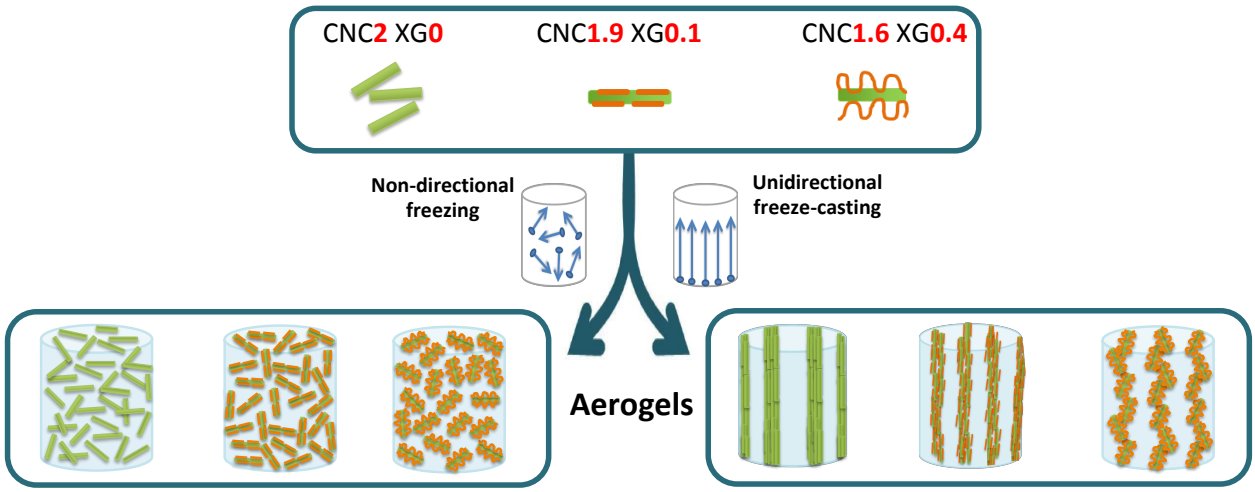

Figure 1: Schematic description of the different aerogels with distinct compositions CNC2 XG0; CNC1.9 XG0.1 and CNC1.6 XG0.4, obtained from both non-directional (left) and unidirectional (right) freezing techniques. In the case of CNC1.9 XG0.1, XG is adsorbed as trains on the surface of CNCs, while CNC1.6 XG0.4 has the XG adsorbed in the form of loops and tails. Blue arrows

show directions of ice crystals growth. XG and CNC dimensions were not scaled for clarity reasons (the gyration radius of XG in solution is larger than the CNC lateral dimensions).

Table 1 summarizes the composition and the characteristics of the aerogels. The aerogels based on 2% CNC or 2% CNC-XG mixtures have densities of *ca*. 19 kg.m^{-3} when prepared by UF, and *ca*. 23 kg.m^{-3} when prepared by NF. This difference can be correlated with the observed slight decrease in the volume of the aerogels prepared by NF, indicating a small shrinkage of the structure during the drying step of the hydrogel.

Table1: Characteristics of the different aerogels (CNC2 XG0, CNC1.9 XG0.1 and CNC1.6 XG0.4) prepared with a final concentration of 2 wt%, by unidirectional freezing (UF) or non-directional freezing (NF).

Aerogel	**Composition**		**Method**	**Density (kg.m^{-3})**	**Void fraction (%)**	**Elastic modulus (kPa)**	**Yield stress (kPa)**	**Herman's orientation factor *f***
	CNC	**XG**						
CNC2 XG0	2%	0%	UF	19±1	98.7	138±69	7.8	0.52
CNC1.9 XG0.1	1.9%	0.1%	UF	18±2	98.8	361±171	28.9	0.40
CNC1.6 XG0.4	1.6%	0.4%	UF	17±1	98.8	610±246	53.3	0.36
CNC2 XG0	2%	0%	NF	23±1	98.5	10±1	_	0.15
CNC1.9 XG0.1	1.9%	0.1%	NF	23±1	98.5	136 ±12	19.67	0.10
CNC1.6 XG0.4	1.6%	0.4%	NF	23±1	98.5	237±91	9.83	0.18

3.2 Aerogels morphology

The morphologies of the aerogels were investigated by scanning electron microscopy (SEM). Aerogels prepared by NF showed random, or disordered, structures and no significant morphological difference could be evidenced between the different compositions (Fig. SI1). Indeed, when solutions were frozen in the absence of a controlled temperature gradient, the crystals tend to grow with no preferred direction, resulting in isotropic pore structures (Köhnke et al., 2012). Figure 2 shows representative SEM images of the aerogels prepared by UF at increasing CNC/XG concentration ratios (*i.e.* CNC2 XG0, CNC1.9 XG0.1 and CNC1.6 XG0.4). Perpendicular and parallel sections (Fig. 2) of the cylindrical monolith show oriented structures of the aerogels along the temperature gradient direction. UF-generated CNC aerogels exhibited a lamellar pore structure (Fig. 2a), a common morphological feature found in the literature for freeze-cast CNC aerogels (Chau et al., 2016; Dash et al., 2012; Kam et al., 2019; Munier et al., 2016). In contrast, the XG-CNC aerogels displayed alveolar elongated pores (Figs. 2b and 2c), similar to a honeycomb structure (Pan et al., 2016) reminiscent of the morphology reported for cellulose nanofiber (CNF) aerogels (Donius, Liu, Berglund, & Wegst, 2014; Munier et al., 2016; Pan et al., 2016). Increasing XG concentration induced an increase in pore size. Assuming that the alveoli shape is almost circular, based on SEM images, the average cell dimension was estimated at 46 μm (±15 μm) and 127 μm (±23 μm) for CNC1.9 XG0.1 and CNC1.6 XG0.4 aerogels, respectively. In both cases, the pores have been found to be open since windows between the pores are clearly visible, as commonly obtained for ice-templated materials. This was also confirmed by the confocal images as discussed in the next section. The change from lamellar to alveolar morphology in the presence of XG has been related to an increase in the viscosity of the CNC/XG colloidal dispersion.[40] Accordingly, we recently reported that simple mixing of XG and CNC leads

295 to an increase of the viscosity of the dispersion and the formation of hydrogels (Talantikite,
296 Gourlay, Gall, & Cathala, 2019). We have proposed that gelation is due to steric stabilization when
297 the CNC surface are crowded while cross-linking might occur at lower CNC/XG to form microgels
298 in agreement with our previous reports (Dammak et al., 2015; Villares et al., 2015). These
299 variations in the physicochemical environment may change ice nucleation as well as the growth of
300 ice crystals. The full understanding of the link between CNC/XG mixture rheology properties and
301 ice nucleation and growth would require a dedicated and in-depth study that is beyond the scope
302 of the current work (Zhang & Liu, 2018). This finding is reminiscent of a recent study on the
303 preparation of XG-CNC aerogels by 3D printing coupled with UF (Kam et al., 2019) showing that
304 higher relative amounts of XG increase the viscosity of the CNC/XG suspensions and induce a
305 morphological evolution of the ice crystals, yielding to a transition from a lamellar aerogel
306 morphology a to tubular morphology or to a disordered morphology at the highest concentrations
307 (Buchtova & Budtova, 2016; Kam et al., 2019).

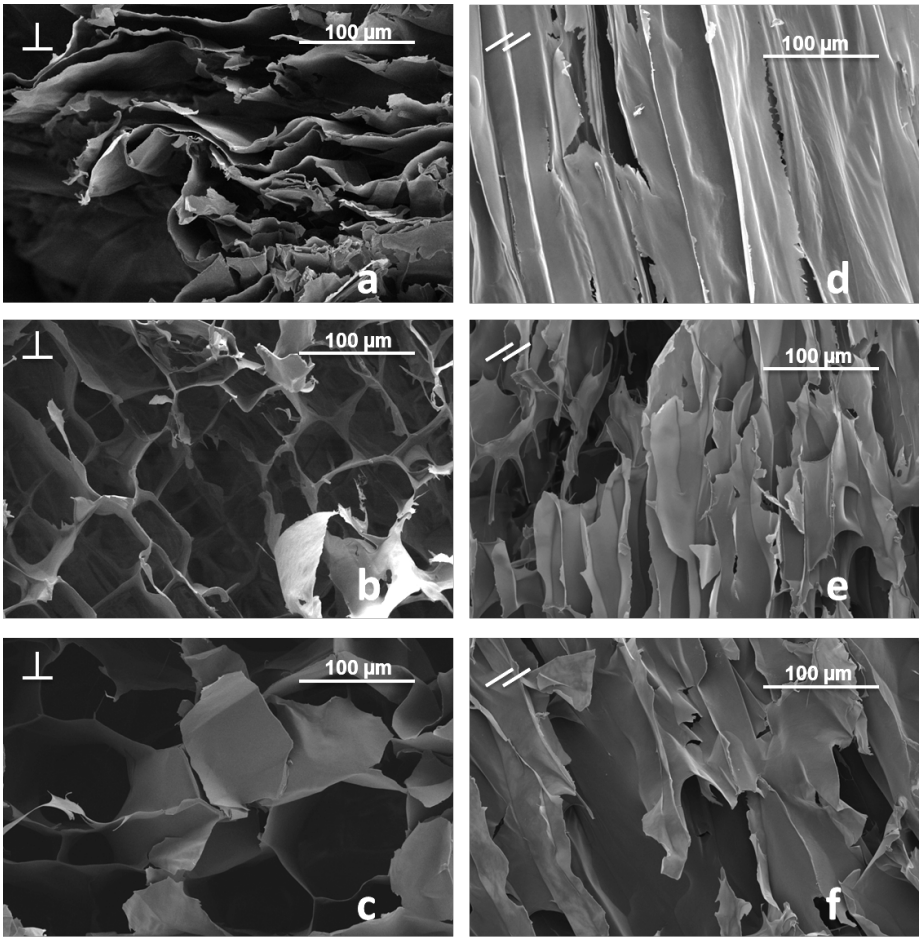

Figure 2: SEM micrographs of CNC and CNC/XG aerogels prepared by UF. Compositions of the aerogels are given as: (a, d) CNC2 XG0; (b, e) CNC1.9 XG0.1; (c, f) CNC1.6 XG0.4. Slices are cut perpendicular (a, b, c) and parallel (d, e, f) to the freezing direction.

Aerogel morphologies were also investigated by confocal microscopy and XG was tagged with rhodamine B isothyocyanate (RITC) and CNC with fluorescein isothyocyanate (FITC). Typical morphologies of the aerogels prepared by UF are depicted in Figure 3. The lowest XG ratio sample (CNC1.9 XG0.1) yields more disordered pores than the high XG ratio (CNC1.6 XG0.4) aerogels in terms of both pore section dimensions and pore alignment. In particular, the

CNC1.6 XG0.4 sample displays polyhedral pore cross-sections suggesting the growth of uniform ice columns during ice templating. The CNC1.9 XG0.1 sample displays a more disordered structure suggesting that the ice growth phenomenon is less controlled by the thermal gradient. Confocal microscopy images are in good agreement with SEM observations since larger pores are observed in the case of CNC1.6 XG0.4 samples, in contrast with pores observed at lower CNC/XG ratios. The samples were prepared from a representative zone of the monolith and connections between pores can be observed in both samples. Pore connections are sometimes visible, indicating that the pores are not fully closed. However, it can be stated qualitatively that the CNC1.6 XG0.4 sample has the most continuous wall structure of all samples observed.

CNC1.9 XG0.1

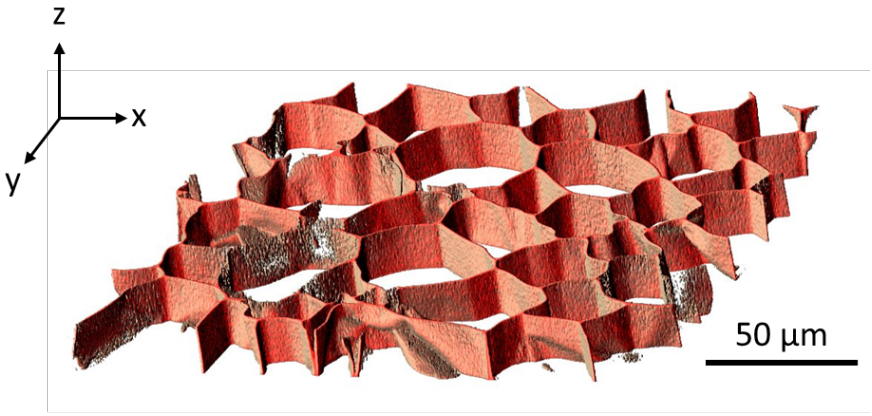

CNC1.6 XG0.4

Figure 3: 3D reconstruction of CNC/XG UF aerogels from confocal microscopy of the XG-RITC channel (top, CNC1.9 XG0.1; bottom, CNC1.6 XG0.4). Aerogel sections were imaged after lyophilization, slicing with a scalpel normal to the ice growth axis and placed in immersion oil for observation. Confocal images of 180*180*15 μm^3 volume sections were acquired in 300 nm z-steps. Reconstruction was conducted in FIJI software using the Volume Viewer plugin (Schindelin et al., 2012).

The segregation of solutes from the initial solution is inherent to ice templating. Since the solubility of each polysaccharide may differ during the freezing-induced segregation, it is critical to assess whether both polymers are co-localized after ice-templating or if some phase separation occurs, and thus to ensure that they reproduce locally the global CNC/XG ratios. Figure SI2 depicts the analysis of the colocalization between the two fluorescence channels for samples CNC1.9 XG0.1 and CNC1.6 XG0.4. In both cases a positive correlation between the intensities of the two channels, as defined by the Pearson's R value can vary from -1 for perfect negative correlation to +1 for perfect correlation. Here, the Pearson's R value was 0.74 and 0.84 for high- and low-XG ratios, respectively indicating that CNC and XG are distributed homogeneously throughout the imaged sample section and that no segregation occurs.

3.3 CNC orientation

X-Ray diffraction (XRD) was used to determine the azimuthal intensity profiles of the (200) ring of crystalline cellulose I (Fig. SI3 and Fig. 4). When the X-ray beam is perpendicular to the freezing direction, aerogels prepared by UF show diffraction patterns with a typical fiber diffraction profile due to preferred orientation. This is observed as two distinct peaks at approximately 90° and 270° in the azimuthal intensity profiles (Fig. 4a). This indicates that CNC

353 are oriented along the freezing direction when the samples are produced by UF. When the X-ray
354 beam is parallel to the aerogel's axis, an almost flat azimuthal profile is observed (Fig. 4c). Similar
355 results were reported in previous studies for 0.5% CNF and 1.5% CNC aerogels prepared by
356 directional freeze-casting, showing anisotropic profiles of X-ray diffraction patterns and indicating
357 that cellulose nanoparticles are also highly oriented along the freezing gradient (Munier et al.,
358 2016). These diffractograms strongly contrast with the quasi-isotropic diffractograms of non-
359 directional freeze-cast NF aerogels that display minimal azimuthal intensity variations (Fig. 4b
360 and d).
361 The degree of orientation of CNC can be quantified by Herman's orientation factor, f (Hermans,
362 Hermans, Vermaas, & Weidinger, 1946). f is calculated and presented in Table 1 for the different
363 aerogels. The aerogels prepared by NF are characterized by very low Herman's factors compared
364 to aerogels prepared by UF (Table1), confirming that the UF aerogels bear oriented CNC within
365 their walls. It has been proposed that CNC can align through compaction during freeze-drying or
366 by the growing ice front during unidirectional freezing (Han, Zhou, Wu, Liu, & Wu, 2013). Indeed,
367 during freezing of aqueous suspensions of CNCs, water is frozen into ice crystals and most CNC
368 above a critical size are trapped by the moving ice front and confined in interstitial spaces between
369 the ice crystals (Deville, Saiz, Nalla, & Tomsia, 2006; Han et al., 2013). CNC aerogels prepared
370 by UF display a higher alignment than XG/CNC aerogels. We correlate the presence of XGs in
371 these aerogels to their less-aligned microstructure. In a previous study dedicated to CNC and CNF
372 aerogels prepared by UF, it was shown that cellulose particles were oriented when the
373 concentration of the dispersion was above a critical value (0.2 wt% for CNC and 0.08 wt% for
374 CNF) (Munier et al., 2016). CNF were slightly less oriented compared to CNC in the freeze-cast
375 aerogels, which was attributed to the rod-like shape of the rigid CNC compared to the more flexible

CNF (Munier et al., 2016). Similar assumptions can be made here. Rigid CNC can easily reorient due to a local concentration increase or shearing during ice growth, as opposed to a CNC/XG network that likely forms a less mobile assembly, with collective motion.

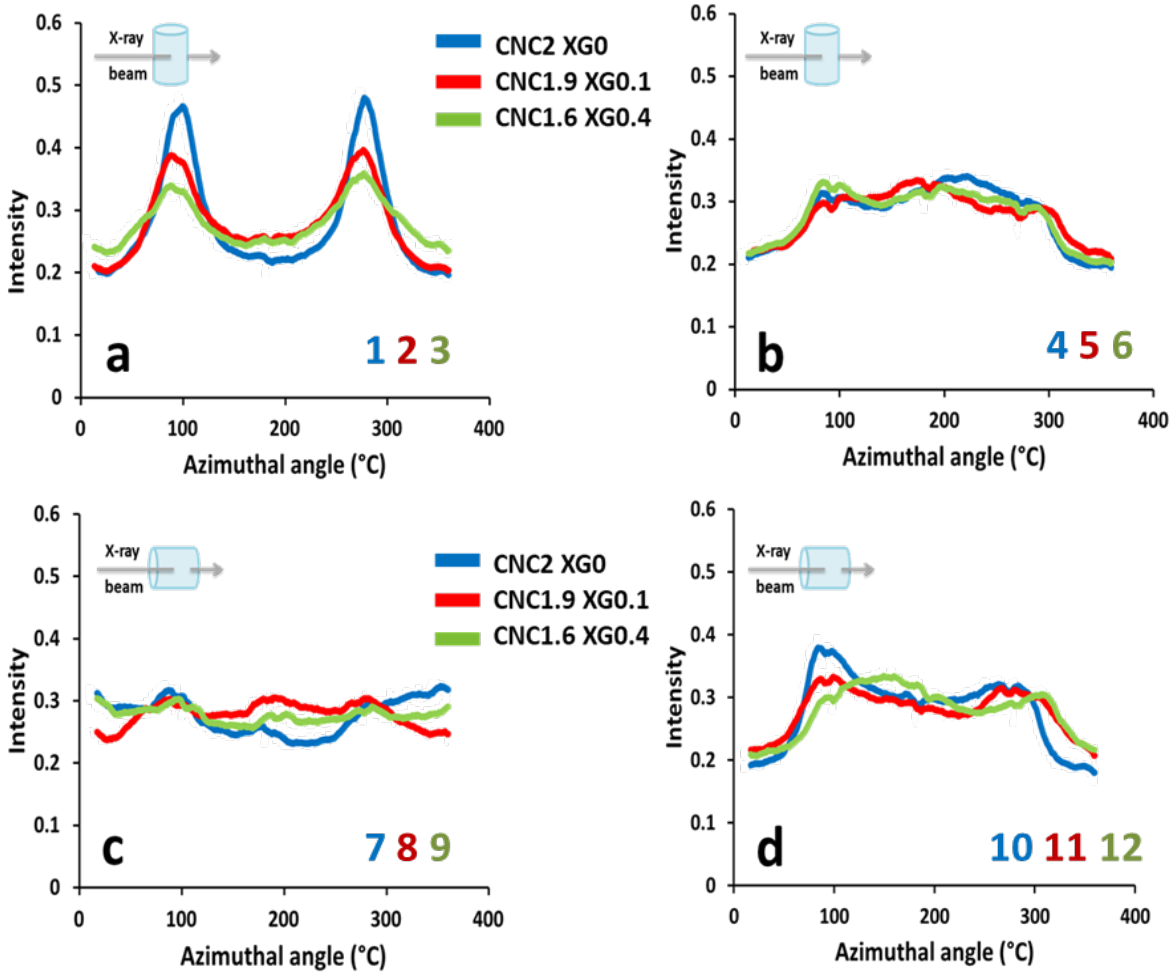

Figure 4: X-ray diffraction investigation showing azimuthal intensity profiles of the aerogels (CNC2 XG0, CNC1.9 XG0.1 and CNC1.6 XG0.4) prepared by UF (a, c) or NF (b, d), where the X-ray beam is perpendicular (a, b) or parallel to the freezing direction (c, d). 2D detector images (Figure SI3) of the aerogels are given above the azimuthal intensity profiles.

3.4 Mechanical properties

The mechanical properties of the aerogels were studied by uniaxial compression in the longitudinal direction both on UF and NF samples. Figure 5 shows representative compression curves for the aerogels prepared by UF (Figure 5a) and NF (Figure 5b). The aerogels prepared by UF (Figure 5a) show typical compressive stress–strain curves where three regions can be distinguished (Gibson & Ashby, 1999). The first linear region at low strains results from the elastic deformation from which the elastic modulus can be determined. A yield stress corresponding to the elastic limit at the end of the linear region is determined (Table 2). The second region with a gradual increase in the stress value corresponds to the cell collapse plateau. Finally, a steep increase in the stress at strains larger than *ca*. 60% is observed in the densification region where the pore cell walls merge. For aerogels prepared by NF (Figure 5b), the stress-strain curves present a less defined elastic region at low strains (the determination of yield stress is not possible for CNC2 XG0), after which it progressively increases until it reaches a densification region.

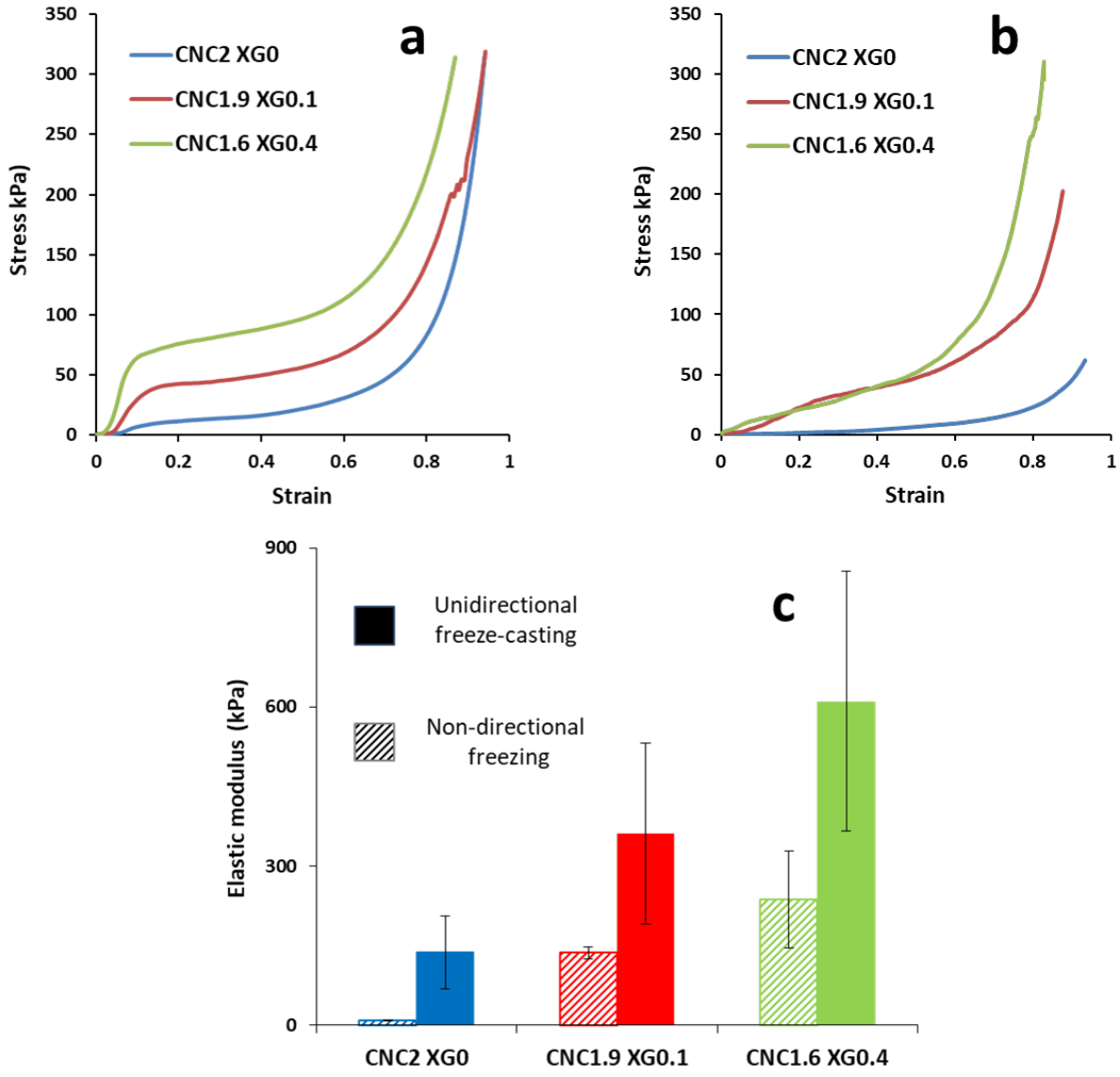

399

400

401 Figure 5: Typical stress-strain uniaxial compression curves for aerogels (CNC2 XG0; CNC1.9
402 XG0.1; CNC1.6 XG0.4) prepared by UF (a) and NF (b). A rod diagram comparing the longitudinal
403 elastic moduli (kPa) resulting from the uniaxial compression of the aerogels (CNC2 XG0; CNC1.9
404 XG0.1; CNC1.6 XG0.4) prepared by UF and NF (c).

405 The values measured for UF-generated samples are in the same range (100-600 kPa) as
406 those reported in the literature and larger than for those prepared by NF(Pääkkö et al., 2008;

Sehaqui, Salajková, Zhou, & Berglund, 2010). In particular, CNC2 XG0 aerogels prepared by UF have a longitudinal elastic modulus 14 times higher than CNC2 XG0 prepared by NF (Table 1 & Fig. 4). However, the influence of the freezing method is less pronounced with CNC1.9 XG0.1 and CNC1.6 XG0.4 aerogels, with only a 2.5 factor between longitudinal elastic moduli of UF and NF samples. Our results clearly demonstrate that the addition of XG to CNC improved the rigidity of the aerogels due to XG adsorption. This effect is magnified when pores are oriented in the direction of the compression, due a high lineic relative density on UF samples compared to NF samples. In fact, for aerogels prepared by UF, an elastic modulus of 610 kPa is reached for CNC1.6 XG0.4, which is almost two times higher than CNC1.9 XG0.1 (360 kPa) and four times higher than CNC2 XG0 (138 kPa). Concomitantly, the addition of XG increases the yield stress 7 times, from 7.8 kPa for CNC2 XG0 to 53.3 kPa for CNC1.6 XG0.4. This result indicates that XG increases the resistance to the deformation before irreversible damage. This result is noteworthy since it highlights the importance of XG for the cell wall mechanical resistance, a resistance that is often assumed to be provided by cellulose alone. As a comparison, the incorporation of XG in microfibrillated cellulose (MFC) aerogels (2/8 XG/MFC), with an equivalent total dried mass fraction of 2 %, increased their elastic modulus from 440 kPa to 970 kPa (Xu et al., 2013). This result is in the same range as CNC1.6 XG0.4 whereas MFC have considerably higher aspect ratios than CNC. It is also important to point out that the highest modulus is obtained for the sample where CNC orientation degree is the lowest, suggesting that such this alignment is detrimental to compression properties, in accordance with the current knowledge on compression wood (high microfibril angle) with respect to tension wood (low microfibril angle, strong longitudinal alignement).

3.4 Dissolution in water

Aerogels prepared by UF were examined after immersion in ink-colored water (Fig. 6). The cylindrical shape of pure CNC aerogels was quickly lost upon swelling (Fig. 6b). The dispersion took 5 h for CNC1.9 XG0.1 (Fig. 6c), whereas CNC1.6 XG0.4 retained its structural cohesion for up to two weeks after immersion (Fig. 6 d, e). This experiment, despite its simplicity, clearly demonstrates the efficiency of the CNC/XG cross-links. These cross-links have a similar effect on the water stability of the aerogels than covalent cross-links. For instance, a previous report on xylan/CNC aerogels prepared by UF showed that xylan oxidation was necessary to create covalent bonds during drying and therefore to obtain water-stable aerogels, whereas unmodified xylan led to composite aerogels that were easily dispersed in water (Köhnke et al., 2014) Similar results can therefore be obtained without the use of specific chemicals.

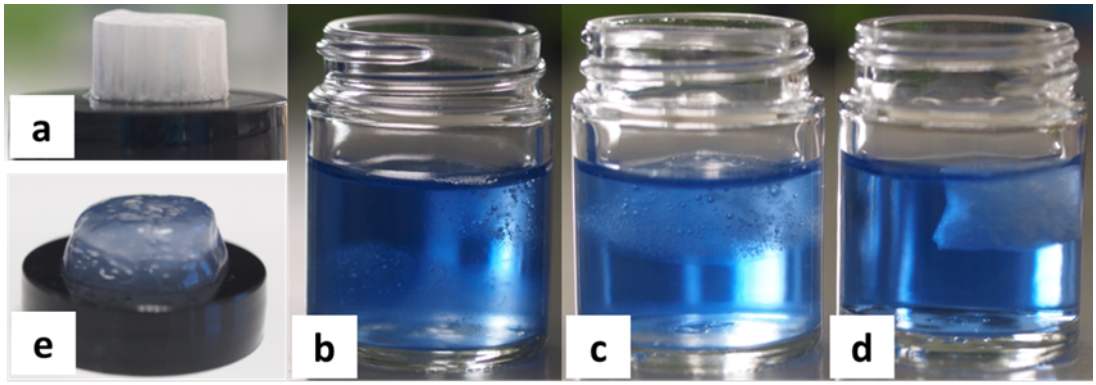

Figure 6: Photo illustrating an example of the freeze-cast aerogel before immersion in water (a) and after 4 hours (b, c, d) and 2 weeks (e). The aerogels used in this experiment were prepared by UF and consist of CNC2 XG0 (b), CNC1.9 XG0.1 (c) and CNC1.6 XG0.4 (d, e).

448

449 4 DISCUSSION

450 Aerogels of CNC/XG mixtures have been successfully prepared by employing the
451 unidirectional freeze-casting technique, where the pore morphology of the material was controlled
452 by the freezing conditions. It has been shown that the addition of XG changed the morphology of
453 the CNC aerogels from lamellar to alveolar. The pore size was larger when higher XG amounts
454 were present in the aerogel. Uniaxial compression tests showed that UF provided stronger aerogels
455 than non-directional freezing. Non-directional freezing resulted in random unordered porous
456 structures. This result is in agreement with previous works showing that aligning cellulose or chitin
457 nanofibers can enhance both the stiffness and the strength of dense films (Gindl & Keckes, 2007;
458 Kvien & Oksman, 2007; Sehaqui et al., 2012) or filaments (Hakansson et al., 2014; Torres-
459 Rendon, Schacher, Ifuku, & Walther, 2014). It has been also shown that the freeze-cast aerogels
460 with the highest relative amount of XG (CNC1.6 XG0.4) bore the largest pores. These pores were
461 alveolar. These samples also had the highest elastic modulus compared to the other aerogels with
462 lower amounts of XG. Hence, the distinct mechanical behaviors of the aerogels prepared by UF
463 and NF can be explained by the difference in structural morphologies of the aerogels. It has to be
464 noticed that the freezing rate, that is markedly different for UF and NF methods, may impact the
465 setting of CNC-XG interactions and therefore contribute to the difference in mechanical properties.
466 Our results are consistent with literature results related to xylan-CNC aerogels, showing that the
467 strong anisotropy of the porous structure of the UF-generated structure induced greater mechanical
468 properties than random porosity obtained by NF, and that samples possessing larger pores were
469 stronger and stiffer than samples containing smaller pores (Köhnke et al., 2012).

470 X-ray diffraction investigation showed that XG has a negative effect on CNC orientation in the ice
471 crystal growth direction. According to Herman's factor, CNC are less aligned in CNC1.6 XG0.4,

while the best mechanical properties are obtained with this composition. The alignment of CNC is therefore not the major factor of the improved mechanical properties of XG-CNC aerogels prepared by freeze-casting. The formation of a co-continuous network of rigid nanocrystals relying on hydrogen bonding and van der Waals interactions between XG and CNC could be the reason for the observed mechanical improvement, since relatively isotropic aerogels were affected that way. This co-continuous network is also efficient at providing a much better resistance to water immersion as illustrated by the CNC1.6 XG0.4 sample. In contrast, simply percolated CNC aerogels without any XG addition are prone to water redispersion due to the lack of intimate binding between the rigid CNC rods alone, probably due to steric effects.

It is known that the high stiffness of CNC reinforced composites results from the hydrogen-bonding forces that hold the percolating network of fibers together (Buchtova & Budtova, 2016; Favier, Chanzy, & Cavaille, 1995). (Capadona, Shanmuganathan, Tyler, Rowan, & Weder, 2008). However, this stiffness increase comes at the price of interparticle binding in wet environments, a function that the matrix provides. The influence of a co-continuous polymer network on moisture resistance was also observed when cellulose was used instead of XG (Lourdin et al., 2016). However the ease of use of XG constitutes a breakthrough in that this process is water-based and doesn't require to use hazardous ionic liquids or chemical reagents.

This behavior of XG is well consistent with previous results on XG and bacterial nanocellulose hydrogel as a cell wall analogues, where tethers of XG between the cellulose fibers have been evidenced (Lopez-Sanchez et al., 2015). In addition, these XG segments were still present after extensive washing of the samples, indicating that XG interacts strongly with the cellulose fibers in water-saturated environments. It was also shown that XG and bacterial nanocellulose hydrogels were approximately half the thickness of bacterial nanocellulose-only samples produced after the

same fermentation time, likely due to the effect of xyloglucan crosslinks bringing the cellulose fibers closer and leading to a more compact structure (Lopez-Sanchez et al., 2015).

In fact, the challenge of creating aerogels from CNCs relies on the ability to form effective water-stable bonds between individual rigid particles. CNC aerogels based on hydrogen bonding and physical cross-links may suffer in mechanical performance and may permanently collapse or redisperse in water. Thus, in the most of the previous studies that examine CNC aerogels, CNCs were used as a nanofiller within a polymer matrix to give a reinforced gel (Coulibaly et al., 2013; Xu et al., 2013; Yang, Bakaic, Hoare, & Cranston, 2013) or used alone to form a networked structure by chemical or physical cross-linking (Dash et al., 2012; Fumagalli, Sanchez, Boisseau, & Heux, 2013; Heath & Thielemans, 2010; Yang & Cranston, 2014). In this work, CNC were cross-linked with XG in water, without any chemical treatment. Moreover, freeze-cast XG-CNC biomimetic aerogels were obtained and showed well-defined architecture and improved mechanical properties. These results provided a better insight into the contribution of XG to the mechanical properties of the plant cell wall and provided promising strategies to design new fully bio-based materials in green synthesis and processing conditions

5 CONCLUSIONS

Novel bioinspired CNC/XG aerogels processed by the UF were successfully prepared without chemical modification of the biopolymers. The addition of XG changed the morphology of CNC aerogels from lamellar to alveolar, resulting in a honeycomb-like microstructure, and increased both the elastic modulus and the aqueous stability of the aerogels. This can be explained by the interactions between XG chains and CNC rigid nanocrystals, that not only increased the viscosity of the starting mixture but also allowed the formation of strongly interacting CNC/XG

network. Therefore, the CNC/XG ratio has a profound impact of the properties of the aerogels. Increasing the CNC/XG ratio enhances the mechanical properties of the aerogels but decreases the orientation of CNCs within their walls. It is likely that the high relative XG amounts increased the interactions between the CNC, thus limiting their mobility and ability to orient during UF. Such a strengthening of inter-CNC interactions would also explain the enhanced stability of aerogels in water. Importantly, these interactions are mediated by the XG molecules and therefore depend on their conformation on the CNC surface. Based on the different concentration regimes studied here, a loop and tail XG conformation seems more favorable than a train conformation. Altogether the influence of XG on the functional properties of the aerogels is multifaceted and needs to be considered at different scales. These results therefore highlight the possibility to design mechanically-robust and water-stable bioaerogels with well-defined architectures without chemical treatment but relying only the optimal setting of intermolecular forces.

Funding Sources

This work is a contribution to the Labex Serenade program (no. ANR-11-LABX-0064) funded by the "Investissements d'Avenir" programme of the French National Research Agency (ANR) through the A*MIDEX project (no. ANR-11-IDEX-0001-02).

ASSOCIATED CONTENT

AUTHOR INFORMATION

Corresponding Author

*E-mail: bernard.cathala@inrae.fr

Present address

INRAE, UR BIA, F-44316, Nantes, France

541 REFERENCES
542

543 Buchtova, N., & Budtova, T. (2016). Cellulose aero-, cryo- and xerogels: towards understanding
544 of morphology control. *Cellulose,* 23(4), 2585-2595.
545 Burgert, I. (2006). Exploring the micromechanical design of plant cell walls. *American journal of*
546 *botany,* 93(10), 1391-1401.
547 Capadona, J. R., Shanmuganathan, K., Tyler, D. J., Rowan, S. J., & Weder, C. (2008). Stimuli-
548 Responsive Polymer Nanocomposites Inspired by the Sea Cucumber Dermis. *Science,*
549 319(5868), 1370-1374.
550 Chau, M., De France, K. J., Kopera, B., Machado, V. R., Rosenfeldt, S., Reyes, L., Chan, K. J.,
551 Förster, S., Cranston, E. D., & Hoare, T. (2016). Composite hydrogels with tunable
552 anisotropic morphologies and mechanical properties. *Chemistry of Materials,* 28(10),
553 3406-3415.
554 Chu, G., Qu, D., Zussman, E., & Xu, Y. (2017). Ice-assisted assembly of liquid crystalline
555 cellulose nanocrystals for preparing anisotropic aerogels with ordered structures.
556 *Chemistry of Materials,* 29(9), 3980-3988.
557 Cosgrove, D. J. (2005). Growth of the plant cell wall. *Nature reviews molecular cell biology,* 6(11),
558 850.
559 Cosgrove, D. J. (2014). Re-constructing our models of cellulose and primary cell wall assembly.
560 *Current opinion in plant biology,* 22, 122-131.
561 Coulibaly, S., Roulin, A., Balog, S., Biyani, M. V., Foster, E. J., Rowan, S. J., Fiore, G. L., &
562 Weder, C. (2013). Reinforcement of optically healable supramolecular polymers with
563 cellulose nanocrystals. *Macromolecules,* 47(1), 152-160.
564 Dammak, A., Quémener, B., Bonnin, E., Alvarado, C., Bouchet, B., Villares, A., Moreau, C. l., &
565 Cathala, B. (2015). Exploring architecture of xyloglucan cellulose nanocrystal complexes
566 through enzyme susceptibility at different adsorption regimes. *Biomacromolecules,* 16(2),
567 589-596.
568 Dash, R., Li, Y., & Ragauskas, A. J. (2012). Cellulose nanowhisker foams by freeze casting.
569 *Carbohydrate polymers,* 88(2), 789-792.
570 de Belder, A., & Granath, K. (1973). Preparation and Properties of Fluorescein-Labelled Dextrans.
571 *Carbohydrate Research,* 30, 375-378.
572 De France, K. J., Hoare, T., & Cranston, E. D. (2017). Review of Hydrogels and Aerogels
573 Containing Nanocellulose. *Chemistry of Materials,* 29(11), 4609-4631.
574 Deville, S. (2008). Freeze-casting of porous ceramics: a review of current achievements and issues.
575 *Advanced Engineering Materials,* 10(3), 155-169.
576 Deville, S. (2010). Freeze-casting of porous biomaterials: structure, properties and opportunities.
577 *Materials,* 3(3), 1913-1927.
578 Deville, S., Saiz, E., Nalla, R. K., & Tomsia, A. P. (2006). Freezing as a path to build complex
579 composites. *Science,* 311(5760), 515-518.
580 Deville, S., Saiz, E., & Tomsia, A. P. (2006). Freeze casting of hydroxyapatite scaffolds for bone
581 tissue engineering. *Biomaterials,* 27(32), 5480-5489.
582 Donius, A. E., Liu, A., Berglund, L. A., & Wegst, U. G. (2014). Superior mechanical performance
583 of highly porous, anisotropic nanocellulose–montmorillonite aerogels prepared by freeze
584 casting. *Journal of the mechanical behavior of biomedical materials,* 37, 88-99.
585 Favier, V., Chanzy, H., & Cavaille, J. (1995). Polymer nanocomposites reinforced by cellulose
586 whiskers. *Macromolecules,* 28(18), 6365-6367.

587 Fricke, J., & Tillotson, T. (1997). Aerogels: production, characterization, and applications. *Thin*
588 *solid films,* 297(1-2), 212-223.
589 Fumagalli, M., Sanchez, F., Boisseau, S. M., & Heux, L. (2013). Gas-phase esterification of
590 cellulose nanocrystal aerogels for colloidal dispersion in apolar solvents. *Soft Matter,*
591 9(47), 11309-11317.
592 Ghorbani, F., Nojehdehian, H., & Zamanian, A. (2016). Physicochemical and mechanical
593 properties of freeze cast hydroxyapatite-gelatin scaffolds with dexamethasone loaded
594 PLGA microspheres for hard tissue engineering applications. *Materials Science and*
595 *Engineering: C,* 69, 208-220.
596 Gibson, L. J., & Ashby, M. F. (1999). *Cellular solids: structure and properties*: Cambridge
597 university press.
598 Gindl, W., & Keckes, J. (2007). Drawing of self-reinforced cellulose films. *Journal of Applied*
599 *Polymer Science,* 103(4), 2703-2708.
600 Hakansson, K. M. O., Fall, A. B., Lundell, F., Yu, S., Krywka, C., Roth, S. V., Santoro, G., Kvick,
601 M., Wittberg, L. P., Wagberg, L., & Soderberg, L. D. (2014). Hydrodynamic alignment
602 and assembly of nanofibrils resulting in strong cellulose filaments. *Nature*
603 *Communications,* 5.
604 Han, J., Zhou, C., Wu, Y., Liu, F., & Wu, Q. (2013). Self-assembling behavior of cellulose
605 nanoparticles during freeze-drying: effect of suspension concentration, particle size, crystal
606 structure, and surface charge. *Biomacromolecules,* 14(5), 1529-1540.
607 Heath, L., & Thielemans, W. (2010). Cellulose nanowhisker aerogels. *Green Chemistry,* 12(8),
608 1448-1453.
609 Hermans, J., Hermans, P., Vermaas, D., & Weidinger, A. (1946). Quantitative evaluation of
610 orientation in cellulose fibres from the X-ray fibre diagram. *Recueil des Travaux*
611 *Chimiques des Pays-Bas,* 65(6), 427-447.
612 Jiménez-Saelices, C., Seantier, B., Grohens, Y., & Capron, I. (2018). Thermal Superinsulating
613 Materials Made from Nanofibrillated Cellulose-Stabilized Pickering Emulsions. *ACS*
614 *applied materials & interfaces,* 10(18), 16193-16202.
615 Kam, D., Chasnitsky, M., Nowogrodski, C., Braslavsky, I., Abitbol, T., Magdassi, S., & Shoseyov,
616 O. (2019). Direct Cryo Writing of Aerogels via 3D Printing of Aligned Cellulose
617 Nanocrystals Inspired by the Plant Cell Wall. *Colloids and Interfaces,* 3(2), 46.
618 Karaaslan, M. A., Tshabalala, M. A., Yelle, D. J., & Buschle-Diller, G. (2011). Nanoreinforced
619 biocompatible hydrogels from wood hemicelluloses and cellulose whiskers. *Carbohydrate*
620 *polymers,* 86(1), 192-201.
621 Kim, K. H., Oh, Y., & Islam, M. F. (2012). Graphene coating makes carbon nanotube aerogels
622 superelastic and resistant to fatigue. *Nature Nanotechnology,* 7(9), 562-566.
623 Klemm, D., Kramer, F., Moritz, S., Lindström, T., Ankerfors, M., Gray, D., & Dorris, A. (2011).
624 Nanocelluloses: a new family of nature-based materials. *Angewandte Chemie International*
625 *Edition,* 50(24), 5438-5466.
626 Köhnke, T., Elder, T., Theliander, H., & Ragauskas, A. J. (2014). Ice templated and cross-linked
627 xylan/nanocrystalline cellulose hydrogels. *Carbohydrate polymers,* 100, 24-30.
628 Köhnke, T., Lin, A., Elder, T., Theliander, H., & Ragauskas, A. J. (2012). Nanoreinforced xylan–
629 cellulose composite foams by freeze-casting. *Green Chemistry,* 14(7), 1864-1869.
630 Kvien, I., & Oksman, K. (2007). Orientation of cellulose nanowhiskers in polyvinyl alcohol.
631 *Applied Physics a-Materials Science & Processing,* 87(4), 641-643.
632 Lakes, R. (1993). Materials with structural hierarchy. *Nature,* 361(6412), 511.

633 Lee, J., & Deng, Y. (2011). The morphology and mechanical properties of layer structured
634 cellulose microfibril foams from ice-templating methods. *Soft Matter,* 7(13), 6034-6040.
635 Lopez-Sanchez, P., Cersosimo, J., Wang, D., Flanagan, B., Stokes, J. R., & Gidley, M. J. (2015).
636 Poroelastic mechanical effects of hemicelluloses on cellulosic hydrogels under
637 compression. *Plos one,* 10(3), e0122132.
638 Lourdin, D., Peixinho, J., Breard, J., Cathala, B., Leroy, E., & Duchemin, B. (2016). Concentration
639 driven cocrystallisation and percolation in all-cellulose nanocomposites. *Cellulose,* 23(1),
640 529-543.
641 Munier, P., Gordeyeva, K., Bergström, L., & Fall, A. B. (2016). Directional freezing of
642 nanocellulose dispersions aligns the rod-like particles and produces low-density and robust
643 particle networks. *Biomacromolecules,* 17(5), 1875-1881.
644 Pääkkö, M., Vapaavuori, J., Silvennoinen, R., Kosonen, H., Ankerfors, M., Lindström, T.,
645 Berglund, L. A., & Ikkala, O. (2008). Long and entangled native cellulose I nanofibers
646 allow flexible aerogels and hierarchically porous templates for functionalities. *Soft Matter,*
647 4(12), 2492-2499.
648 Pan, Z.-Z., Nishihara, H., Iwamura, S., Sekiguchi, T., Sato, A., Isogai, A., Kang, F., Kyotani, T.,
649 & Yang, Q.-H. (2016). Cellulose nanofiber as a distinct structure-directing agent for
650 xylem-like microhoneycomb monoliths by unidirectional freeze-drying. *ACS nano,* 10(12),
651 10689-10697.
652 Saxena, A., Elder, T. J., Pan, S., & Ragauskas, A. J. (2009). Novel nanocellulosic xylan composite
653 film. *Composites Part B: Engineering,* 40(8), 727-730.
654 Scheller, H. V., & Ulvskov, P. (2010). Hemicelluloses. *Annual review of plant biology,* 61.
655 Schindelin, J., Arganda-Carreras, I., Frise, E., Kaynig, V., Longair, M., Pietzsch, T., Preibisch, S.,
656 Rueden, C., Saalfeld, S., Schmid, B., Tinevez, J. Y., White, D. J., Hartenstein, V., Eliceiri,
657 K., Tomancak, P., & Cardona, A. (2012). Fiji: an open-source platform for biological-
658 image analysis. *Nature Methods,* 9(7), 676-682.
659 Sehaqui, H., Mushi, N. E., Morimune, S., Salajkova, M., Nishino, T., & Berglund, L. A. (2012).
660 Cellulose Nanofiber Orientation in Nanopaper and Nanocomposites by Cold Drawing.
661 *ACS applied materials & interfaces,* 4(2), 1043-1049.
662 Sehaqui, H., Salajková, M., Zhou, Q., & Berglund, L. A. (2010). Mechanical performance tailoring
663 of tough ultra-high porosity foams prepared from cellulose I nanofiber suspensions. *Soft*
664 *Matter,* 6(8), 1824-1832.
665 Svagan, A. J., Jensen, P., Dvinskikh, S. V., Furó, I., & Berglund, L. A. (2010). Towards tailored
666 hierarchical structures in cellulose nanocomposite biofoams prepared by freezing/freeze-
667 drying. *Journal of Materials Chemistry,* 20(32), 6646-6654.
668 Szepes, A., Ulrich, J., Farkas, Z., Kovács, J., & Szabó-Révész, P. (2007). Freeze-casting technique
669 in the development of solid drug delivery systems. *Chemical Engineering and Processing:*
670 *Process Intensification,* 46(3), 230-238.
671 Talantikite, M., Gourlay, A., Gall, S.-L., & Cathala, B. (2019). Influence of Xyloglucan Molar
672 Mass on Rheological Properties of Cellulose Nanocrystal/Xyloglucan Hydrogels. *Journal*
673 *of Renewable Materials,* 7(12), 1381--1390.
674 Torres-Rendon, J. G., Schacher, F. H., Ifuku, S., & Walther, A. (2014). Mechanical Performance
675 of Macrofibers of Cellulose and Chitin Nanofibrils Aligned by Wet-Stretching: A Critical
676 Comparison. *Biomacromolecules,* 15(7), 2709-2717.
677 Villares, A., Moreau, C., Dammak, A., Capron, I., & Cathala, B. (2015). Kinetic aspects of the
678 adsorption of xyloglucan onto cellulose nanocrystals. *Soft Matter,* 11(32), 6472-6481.

679 Wicklein, B., Kocjan, A., Salazar-Alvarez, G., Carosio, F., Camino, G., Antonietti, M., &
680 Bergström, L. (2015). Thermally insulating and fire-retardant lightweight anisotropic
681 foams based on nanocellulose and graphene oxide. *Nature Nanotechnology,* 10(3), 277.
682 Xu, X., Liu, F., Jiang, L., Zhu, J., Haagenson, D., & Wiesenborn, D. P. (2013). Cellulose
683 nanocrystals vs. cellulose nanofibrils: a comparative study on their microstructures and
684 effects as polymer reinforcing agents. *ACS applied materials & interfaces,* 5(8), 2999-
685 3009.
686 Yang, X., Bakaic, E., Hoare, T., & Cranston, E. D. (2013). Injectable polysaccharide hydrogels
687 reinforced with cellulose nanocrystals: morphology, rheology, degradation, and
688 cytotoxicity. *Biomacromolecules,* 14(12), 4447-4455.
689 Yang, X., & Cranston, E. D. (2014). Chemically cross-linked cellulose nanocrystal aerogels with
690 shape recovery and superabsorbent properties. *Chemistry of Materials,* 26(20), 6016-6025.
691 Yin, K., Divakar, P., & Wegst, U. G. (2019). Freeze-casting porous chitosan ureteral stents for
692 improved drainage. *Acta biomaterialia,* 84, 231-241.
693 Zhang, Z., & Liu, X.-Y. (2018). Control of ice nucleation: freezing and antifreeze strategies.
694 *Chemical Society Reviews,* 47(18), 7116-7139.

695